AMS Home   Journals Home   Journal Archive   Subscribe   For Authors   Help   Advanced Search | Search | Go |

Full Text View

The Nondeterministic Nature of Kuroshio Penetration and Eddy Shedding in the South China Sea[*]

E. Joseph Metzger and Harley E. Hurlburt

Naval Research Laboratory, Stennis Space Center, Mississippi

ABSTRACT

A $\frac{1}{8}°$, 6-layer Pacific version of the Naval Research Laboratory Layered Ocean Model is used to investigate the nondeterministic nature of Kuroshio intrusion and eddy shedding into the South China Sea (SCS) on annual and interannual timescales. Four simulations, which only differ in the initial state, are forced with 1979–93 European Centre for Medium-Range Weather Forecasts reanalysis 1000 hectopascal (hPa) winds and then continued in 1994–97 with ECMWF operational 1000-hPa winds. The model shows differing amounts of Kuroshio penetration across all four simulations for the yearly means, indicating a large degree of nondeterminism at this timescale. This nondeterminism is quantified by a technique that separates the variability of a model variable into deterministic (caused by direct atmospheric forcing) and nondeterministic (caused by mesoscale flow instabilities) components. Analysis indicates substantial nondeterministic sea surface height and upper-layer velocity variability in the vicinity of Luzon Strait. A quantitative measure of Kuroshio intrusion into the SCS is presented that allows interexperiment comparisons and investigation of interannual variability, and attempts are made to positively correlate it with the oceanic and atmospheric environment. Yearly mean Kuroshio intrusion is not strongly linked to Luzon Strait transports or to changes in the North Equatorial Current bifurcation latitude (which is related to the northward Kuroshio transport east of Luzon). Likewise, no relationship could be found that linked interannual variability of yearly mean Kuroshio intrusion or monsoon season mean Luzon Strait transport with the corresponding zonal or meridional wind components, wind stress magnitude, or wind stress curl. However, there was a close relationship between the mean seasonal cycles of the Luzon Strait transport and the northeast–southwest monsoon. Eddy shedding and deep Kuroshio intrusion are rare events during the period of ECMWF reanalysis forcing, but are persistent features during the ECMWF operational time frame. While the wind stress is consistent across the reanalysis/operational time boundary, large differences exist in the wind stress curl pattern over the Luzon Strait and interior of the SCS basin. For contemporaneous years, the ECMWF operational winds produce higher curl extrema (by a factor of 2) and a much sharper north–south gradient in Luzon Strait. The net effect is to produce more Ekman pumping, a deepening of the thermocline, and a more deeply penetrating Kuroshio during the 1994–97 ECMWF operational forcing time frame. Thus, while normal interannual variations of the wind curl did not produce a deterministic response of simulated Kuroshio intrusion, the marked differences in curl between the two atmospheric products did have a substantial impact.

Options:
- Create Reference
- Email this Article
- Add to MyArchive
- View Correction to this Article
- Search AMS Glossary

Search CrossRef for:
- Articles Citing This Article

Search Google Scholar for:
- E. Joseph Metzger
- Harley E. Hurlburt

1. Introduction

The South China Sea (SCS) is the largest semienclosed marginal sea in the western tropical Pacific Ocean (Fig. 1 ⊙▬). Its main connection with the Pacific Ocean is via Luzon Strait, which is very wide and has a sill depth of approximately 2400 m. The connections to the south are either very narrow (Sibutu Passage in the southern Sulu Sea) or shallow (a 29-m sill depth at Karimata Strait, which connects the Sunda Shelf and the Java Sea). To the north, Taiwan Strait connects the SCS with the East China Sea but it is generally believed that the Taiwan Warm Current flows northward throughout the year (Chuang 1986; Zhao and Fang 1991). Thus, the main interaction of the SCS with the surrounding waters is through Luzon Strait.

Metzger and Hurlburt (1996, hereafter MH) and the present study have considered three major components of upper ocean flow through Luzon Strait. The first one enters Luzon Strait and exits through another strait. It appears as a branch off the Kuroshio into the SCS just north of the Philippine Islands and is the only one of these that contributes to the long-term mean Luzon Strait transport. The second component is due to variations in the volume of water above the thermocline within the SCS. This one has a strong seasonal cycle associated with the northeast–southwest monsoon. Depending upon the direction of the flow, it can appear as a branch off the Kuroshio into the SCS on the southern side of Luzon Strait or as a current feeding into the Kuroshio on the northern side of the strait. The third component appears as a Kuroshio loop or intrusion into the SCS that enters through the southern part of Luzon Strait and exits through the northern part. In relation to the flow through Luzon Strait, MH concentrated on the first two components, while the present study focuses primarily on the third. However, it is not always clear how to sort out observations in relation to these three components as well as locally driven flows. Thus, at times this will not be clear-cut in the subsequent discussions of observational evidence.

The upper ocean circulation within the SCS is dominated by the seasonally reversing monsoon winds, which typically blow from the northeast during boreal winter and from the southwest during boreal summer. Shaw et al. (1999) suggest that the wind stress curl is the main driving force of the circulation in the deep basin of the SCS except near Luzon Strait. Huang et al. (1994) and Fang et al. (1998) indicate a central basin cyclonic (anticyclonic) circulation during the winter (summer) monsoon. In the northern SCS along the shelf break at a depth of 200–400 m, and most likely originating near Hainan Island, the South China Sea Warm Current (SCSWC) flows northeastward, even during the periods of the northeast monsoon (Guan 1978, 1985). However, the existence of the SCSWC is somewhat controversial. Repeated measurements have yet to confirm that this warm current is a permanent feature. Immediately offshore of the SCSWC, Guo et al. (1985) have found an equally strong southwestward flowing current during the winter. The coastal current along Vietnam also responds to the seasonally changing monsoon winds; it flows to the north during the southwest monsoon and to the south during the northeast monsoon (Wyrtki 1961).

a. Hydrographic evidence for Kuroshio intrusion into the SCS

The Kuroshio (Black Stream) originates where the North Equatorial Current (NEC) bifurcates along the eastern coast of the Philippines at approximately 13.5°N; the southward flowing Mindanao Current has a volume transport of approximately 27 Sv (Sv ≡ 10^6 m^3 s^{-1}) at 8°N, while the northward-flowing Kuroshio transport is approximately 14 Sv at 18°N (Qu et al. 1998). As the Kuroshio flows northward and enters the region of Luzon Strait, it has been observed to bypass the strait (Wang and Chern 1996) as well as penetrate deeply into the SCS and shed eddies. When penetrating, the inflow is typically northwestward in the southern Luzon Strait (Balintang Channel). It turns anticyclonically and exits as a northeastward-flowing current in the northern Luzon Strait (Bashi Channel) (Nitani 1972; Huang et al. 1994).

Hydrographic data exist for the northern SCS/Luzon Strait region, but repeated cruises during all seasons are lacking and, thus, the seasonal climatology is not fully known. A few studies are described here, but it should be noted that cruises taken in the same season do not indicate the same degree of Kuroshio intrusion. Thus, they provide evidence that the interaction between this Pacific western boundary current and the SCS is governed by deterministic interannual variability, nondeterministic variability, or a combination of both. Spring (March) cruise data were analyzed by Xu et al. (1995), who found the Kuroshio penetrating to approximately 119°E and mostly in the northern half of the strait, while the autumn (September) cruise data of Guo and Fang (1988) indicated intrusion to about 120°E. As opposed to these one-time cruises, Shaw (1991) looked at historical hydrographic data across all seasons and over a wide region of the northern SCS and found evidence of an intrusion current over the entire continental margin of the northern SCS in late autumn and winter. That study, along with evidence gathered by Shaw (1989), describes the seasonal cycle as follows: (i) from May to September the Kuroshio front meanders into Luzon Strait (an intrusion current may not exist), (ii) from October to January an intrusion current may begin to form and penetrate along the continental margins, and (iii) from February to May the intrusion current decays. Shaw (1991) also suggests that it is unlikely that an inertial current flows hundreds of kilometers into the SCS, but the intrusion current is part of the general circulation of the northern SCS. A more recent study published by Fang et al. (1998) provides a concise description of observational studies related to the Kuroshio intrusion, many of which come from the Chinese literature. These again indicate the variability of the Kuroshio's interaction with the SCS.

Evidence of warm core (anticyclonic) eddies in the northern SCS have been found by Wang and Chern (1987a) and Li et al. (1998). The former study reports an eddy diameter of approximately 200 km, while the latter found an eddy with a diameter of approximately 150 km and a vertical expression as deep as 1000 m. Li et al. (1998) have also performed a hydrographic analysis that suggests the subsurface water of the eddy is of Kuroshio origin, while the surface waters

associated with the ring are believed to consist of entrained SCS waters. Although some eddies have been observed, the hydrographic observations are insufficient to determine how frequently eddies are shed from the main core of the Kuroshio. Clearly, satellite data will be required to answer this question.

b. Dynamical mechanisms for the Kuroshio intrusion

The dynamics that govern the intrusion of the Kuroshio into the SCS are also not clearly understood. A hypothesis promoted by Wang and Chern (1987b) proposes that the Kuroshio intrusion only occurs during the northeast monsoon season as the winds deflect the Kuroshio transport westward into Luzon Strait. Farris and Wimbush (1996) concur with this theory, as they have examined satellite derived sea surface temperature images and linked the intrusion current development process with an integrated supercritical wind stress parameter. However, Shaw (1991) suggests that the general circulation in the northern SCS is probably driven by higher sea level in Luzon Strait. A weakening of this pressure gradient in summer may prevent a strong intrusion current from developing. He also suggests that the intrusion process may be related to the transport of the Kuroshio or the reversal of the wind direction from the northeast in winter to the southwest in summer.

c. Numerical modeling studies of the SCS/Luzon Strait region

Kuroshio intrusion into the SCS has also been studied by employing numerical ocean models of different types, covering different domains, and applying different forcing. The idealized geometry in the model of W. Li et al. (1996) can be applied to Luzon Strait, and it indicates an intrusion current that penetrates deeper when the gap in the western boundary becomes wider or the latitude decreases. Other models that use realistic coastlines have applied winds only for a specific season in an attempt to examine the response of the Kuroshio. For example, Chern and Wang (1998) applied summertime forcing to a very limited area model (10-km resolution) of Luzon Strait and suggest that the retreat of the intrusion current may be related to the northward movement of the strongly stratified SCS waters driven by southwesterly winds, while Li et al. (1993) used wintertime forcing in their ½° barotropic full basin Pacific model and found a branch of the Kuroshio that penetrated as far east as 113°E. Monthly varying forcing was used by R.-F. Li et al. (1996), who noted Kuroshio penetration to at least 116°E in all months. They suggest that variations in the Kuroshio and the whole current system of the Pacific have an important influence on the current entering the SCS via Luzon Strait. Shaw and Chao (1994) used a limited-area model of the SCS region, also with monthly wind forcing, that only produced the Kuroshio intrusion during the winter months; they suggest that summertime intrusion is blocked by the northeastward flow from the Vietnamese coast toward Luzon Strait. They also indicate that most water exchange between the SCS and Pacific is concentrated in the upper 300 m.

A ½° global, 1.5-layer reduced gravity global model was used by MH to study the coupled dynamics of the SCS and Pacific Ocean region. That paper focused mainly on the controlling factors of the mean Luzon Strait transport and its variability. The Kuroshio intrusion was briefly addressed in their Plate 1, which compared the annual mean sea surface height (SSH) from a ½° global model with higher resolution ($\frac{1}{8}$° and $\frac{1}{16}$°) global and Pacific counterparts. They noted that the Kuroshio penetration was pronounced in the ½° model, but much less so at higher resolutions. This is probably due to a much better model representation of the north–south Babuyan and Batan Island chains; namely, the higher horizontal resolution allows more islands to be resolved and included as part of the coastline geometry. This is supported by a finding in Hurlburt and Thompson (1982) that gives a length scale $(\upsilon_c/\beta)^{1/2}$ for westward bending of the Loop Current in the Gulf of Mexico. This means that higher velocity at the core of the current (υ_c) in higher resolution models tends to increase the length scale for westward bending and to reduce the westward bending on a given length scale $<(\upsilon_c/\beta)^{1/2}$, where β is the planetary vorticity. The westward bending is further reduced by the narrower strait at higher resolution. Thus, an accurate representation of the islands and coastlines appears to be one of the critical elements in modeling this region.

Section 2 of this paper provides a description of the Naval Research Laboratory Layered Ocean Model (NLOM) and the associated experiments used in this study. Annual and seasonal means are presented along with a description of the Luzon Strait transport. Next comes a discussion of a quantitative measure of the Kuroshio penetration. This is followed by an investigation of the nondeterministic nature of Kuroshio intrusion with emphasis on interannual timescales. The model sensitivity to wind forcing is discussed in section 5 and a summary completes this work.

2. The numerical model

a. NLOM description

The numerical ocean model used is a primitive equation layered formulation where the equations have been vertically integrated through each layer. The NLOM is a descendent of the model by Hurlburt and Thompson (1980) with significant enhancements by Wallcraft (1991), Wallcraft and Moore (1997), and Moore and Wallcraft (1998). It is available in both reduced-gravity versions, where the lowest layer is infinitely deep and at rest, and finite depth versions, which allow realistic bottom topography. Additionally, NLOM can be run in a hydrodynamic mode (spatially and temporally constant density within each layer) or in a thermodynamic mode (spatially and temporally density within each layer); that is, density is a prognostic variable. A 6-layer, thermodynamic, finite depth model of the Pacific Ocean north of 20°S is used in this study.

The vertically integrated equations of motion used in the volume conserving n-layer finite-depth thermodynamic model are given below, for layers $k = 1, \ldots , n$, with $k = 1$ for the top layer. When k is used to index the model interfaces, $k = 0$ at the surface and $k = n$ at the bottom:

$$\frac{\partial U_k}{\partial t} + \frac{1}{a\cos\theta}\left[\frac{\partial(U_k u_k)}{\partial\phi} + \frac{\partial(V_k u_k\cos\theta)}{\partial\theta} - V_k(u_k\sin\theta + a\Omega\sin2\theta)\right]$$

$$= \max(0, -\omega_{k-1})u_{k-1} + \max(0, \omega_k)u_{k+1} - (\max(0, -\omega_k) + \max(0, \omega_{k-1}))u_k + \max(0, -C_M\omega_{k-1})(u_{k-1} - u_k)$$

$$+ \max(0, C_M\omega_k)(u_{k+1} - u_k) - \frac{h_k}{a\cos\theta}\left[\sum_{j=1}^{n}\left(G_{kj}\frac{\partial(h_j - H_j)}{\partial\phi} + h_j\frac{\partial G_{kj}}{\partial\phi}\right) - \frac{g}{\rho_o}\left(\sum_{j=1}^{k-1}h_j + \frac{h_k}{2}\right)\frac{\partial\rho_k}{\partial\phi}\right] + (\tau_{\phi_{k-1}} - \tau_{\phi_k})/\rho_o$$

$$+ \frac{A_H}{a^2\cos^2\theta}\left[\frac{\partial(h_k e_{\phi\phi_k}\cos\theta)}{\partial\phi} + \frac{\partial(h_k e_{\phi\theta_k}\cos^2\theta)}{\partial\theta}\right]$$

$$\frac{\partial V_k}{\partial t} + \frac{1}{a\cos\theta}\left[\frac{\partial(U_k v_k)}{\partial\phi} + \frac{\partial(V_k v_k\cos\theta)}{\partial\theta} + U_k(u_k\sin\theta + a\Omega\sin2\theta)\right]$$

$$= \max(0, -\omega_{k-1})v_{k-1} + \max(0, \omega_k)v_{k+1} - (\max(0, -\omega_k) + \max(0, \omega_{k-1}))v_k + \max(0, -C_M\omega_{k-1})(v_{k-1} - v_k)$$

$$+ \max(0, C_M\omega_k)(v_{k+1} - v_k) - \frac{h_k}{a}\left[\sum_{j=1}^{n}\left(G_{kj}\frac{\partial(h_j - H_j)}{\partial\phi} + h_j\frac{\partial G_{kj}}{\partial\phi}\right) - \frac{g}{\rho_o}\left(\sum_{j=1}^{k-1}h_j + \frac{h_k}{2}\right)\frac{\partial\rho_k}{\partial\theta}\right] + (\tau_{\theta_{k-1}} - \tau_{\theta_k})/\rho_o$$

$$+ \frac{A_H}{a^2\cos^2\theta}\left[\frac{\partial(h_k e_{\phi\theta_k}\cos\theta)}{\partial\phi} + \frac{\partial(h_k e_{\theta\theta_k}\cos^2\theta)}{\partial\theta}\right]$$

$$\frac{\partial h_k}{\partial t} + \nabla\cdot\mathbf{V}_k = \omega_k - \omega_{k-1} - \hat{K}_{H_4}\nabla^2[\nabla^2(h_k - H_k)] - \left(\frac{h_k}{\rho_k}\frac{\widehat{\partial\rho_k}}{\partial t} - \frac{\overline{h_k}\,\widehat{\partial\rho_k}}{\rho_k\,\partial t}\right)$$

$$\frac{\partial\rho_k}{\partial t} + \mathbf{v}_k\cdot\nabla\rho_k = \frac{\widehat{\partial\rho_k}}{\partial t} + \frac{\max(0, \omega_k)}{h_k}\max(0, \rho_{k+1} - \rho_k - \Delta\rho_k) - \frac{\max(0, -\omega_{k-1})}{h_k}\max(0, \rho_k - \rho_{k-1} - \Delta\rho_{k-1})$$

$$\frac{\widehat{\partial\rho_k}}{\partial t} = \frac{H_o}{h_k}\sigma_\rho(\hat{\rho}_k - \rho_k) - \delta_{1k}\frac{Q}{c_p\rho_o h_1}\frac{\partial\rho_1}{\partial T} + \frac{1}{h_k}(\nabla\cdot(h_k\nabla))\left[K_H\rho_k - \frac{K_{H_4}}{h_k}(\nabla\cdot(h_k\nabla))\rho_k\right],$$

(Click the equation graphic to enlarge/reduce size)

where

A_H coefficient of horizontal eddy viscosity

C_b coefficient of bottom friction

C_k coefficient of interfacial friction

C_M coefficient of additional interfacial friction associated with entrainment

$D(\phi, \theta)$ total depth of the ocean at rest

$$\nabla\cdot\mathbf{F} = \frac{1}{a\cos\theta}\frac{\partial F_\phi}{\partial\phi} + \frac{1}{a\cos\theta}\frac{\partial F_\theta\cos\theta}{\partial\theta}$$

$$G_{kj} = \begin{cases} g, & \text{for } j \geq k \\ g - g(\rho_k - \rho_j)/\rho_o, & \text{for } j < k \end{cases}$$

H_k kth layer thickness at rest

$$H_n = D(\phi, \theta) - \sum_{j=1}^{n-1}H_j$$

H_o constant reference layer thickness

K_H coefficient of horizontal density diffusivity

K_{H_4} coefficient of biharmonic horizontal density diffusivity

$\hat{K}_{H_4}$ coefficient of biharmonic horizontal layer thickness diffusivity

Q total surface heat flux

T_1 layer 1 temperature climatology

$\mathbf{V}_k = h_k \mathbf{v}_k = \mathbf{e}_\phi U_k + \mathbf{e}_\theta V_k$

$W_k(\phi, \theta)$ kth interface weighting factor for global vertical mixing designed to conserve mass within a layer in compensation for explicit vertical mixing due to $h_k < h_k^+$

$\overline{X(\phi, \theta)}$ domainwide area average of X

a radius of the earth (6371 km)

c_p coefficient of specific heat for seawater

$\mathbf{e}_k$ angular deformation tensor

$$e_{\phi\phi k} = \frac{\partial}{\partial \phi}\left(\frac{u_k}{\cos\theta}\right) - \cos\theta \frac{\partial}{\partial\theta}\left(\frac{v_k}{\cos\theta}\right) = -e_{\theta\theta k}$$

$$e_{\phi\theta k} = \frac{\partial}{\partial \phi}\left(\frac{v_k}{\cos\theta}\right) + \cos\theta \frac{\partial}{\partial\theta}\left(\frac{u_k}{\cos\theta}\right) = e_{\theta\phi k}$$

g acceleration due to gravity

h_k kth layer thickness

h_k^+ kth layer thickness at which entrainment starts

h_k^- kth layer thickness at which detrainment starts

$\max(A, B)$ use the maximum value of the arguments A and B

t time

$\mathbf{v}_k$ kth layer velocity $(=\mathbf{e}_\phi u_k + \mathbf{e}_\theta v_k)$

$$\nabla\Phi = \frac{1}{a\cos\theta}\frac{\partial\Phi}{\partial\phi}\mathbf{e}_\phi + \frac{1}{a}\frac{\partial\Phi}{\partial\theta}\mathbf{e}_\theta$$

$$\nabla^2\Phi = \frac{1}{a^2\cos^2\theta}\frac{\partial^2\Phi}{\partial\phi^2} + \frac{1}{a^2\cos\theta}\frac{\partial}{\partial\theta}\left(\frac{\partial\Phi}{\partial\theta}\cos\theta\right)$$

Ω earth's angular rotation rate (7.292205×10^{-5} s^{-1})

ϕ longitude

θ latitude

ρ_k kth-layer density

$\hat{\rho}_k(\phi, \theta)$ kth-layer density climatology

$\Delta\rho_k$ kth-interface minimum density shear

ρ_o constant reference density

$$\frac{\partial\rho_1}{\partial T} = 0.0757 + 0.00946\hat{T}_1$$

σ_ρ reference coefficient of density climatology relaxation

$$\tau_w \quad \text{wind stress}$$

$$\omega_k = \begin{cases} 0, & \text{for } k = 0, n \\ \omega_k^+ - \omega_k^- - W_k \hat{\omega}_k, \\ & \text{for } k = 1, \cdots, n - 1 \end{cases}$$

$$\omega_k^+ = \tilde{\omega}_k (\max(0, h_k^+ - h_k)/h_k^+)^2$$

$$\omega_k^- = \tilde{\omega}_k (\max(0, h_k - h_k^-)/h_k^+)^2$$

$$\hat{\omega}_k = \overline{(\omega_k^+ - \omega_k^-)}/\overline{W_k}$$

$$\tilde{\omega}_k \quad k\text{th-interface reference vertical mixing ve-locity}$$

The model boundary conditions are kinematic and no slip. No heat flux forcing is applied in the experiments used here. Table 1 ⊙ defines the nonvarying model parameters.

The model domain covers the Pacific Ocean from 20°S to 62°N in latitude and 109.125°E to 77.21°W in longitude, but here the focus is on the subregion of the SCS. The horizontal resolution of each prognostic model variable is $\frac{1}{8}$° in latitude by 45/256° in longitude. The model contains horizontal mixing in the form of Laplacian friction and allows vertical exchange of momentum, mass, and heat across the interfaces. The model permits ventilation of the interfaces between the layers (outcropping). Vertical mixing (entrainment) is applied when a layer thins beyond a prescribed minimum layer thickness (h_k^+) and water from the layer below is entrained at a velocity ($\tilde{\omega}_k$) needed to prevent nonpositive layer thickness. Volume is conserved within a layer by domainwide vertical mixing using a weighting scheme based on oxygen saturation as discussed in Shriver and Hurlburt (1997). Horizontal density gradients within a layer can be modified by advection, diffusion, entrainment, heating (not used), and relaxation to an annual mean density climatology, here based on Levitus and Boyer (1994) and Levitus et al. (1994).

The 1/12° ETOP05 bottom topography (NOAA 1986) was used in the model with some modifications. It was interpolated to the model grid, then smoothed twice with a nine-point real smoother to reduce energy generation at small scales that are poorly resolved by the model. The 200-m isobath generally defines the model land–sea boundary but there are some exceptions, namely the Taiwan Strait, which has been opened at the 25-m isobath, and two interior Philippines passages, Leyte Gulf (10.5°N, 125.5°E) and San Bernadino Strait (8.0°N, 124.5°E), are opened. The model does not allow the interfaces to intersect the bottom topography, so the topography must be confined to the lowest layer. Thus, in order to prevent unrealistically high transport through Taiwan Strait, depth-weighted friction is applied (as discussed in the appendix of MH). In general, flow is constrained to near zero in layers completely below the sill depth. The model produces a net northward Taiwan Strait transport of 0.7 ± 0.3 Sv in comparison to the 2.1 Sv estimate of Zhao and Fang (1991). The model boundaries are closed along 20°S, at the southern Indonesian archipelago, and at the Sunda Shelf in the southwest SCS. The Sunda Shelf region covers a large geographical area, but it is very shallow. The Karimata Strait that joins the Sunda Shelf with the Java Sea is approximately ¼° wide at the 25-m isobath and has a sill depth of 29 m. Metzger and Hurlburt has shown that closing the Pacific to Indian Ocean throughflow and the Sunda Shelf does not significantly impact the flow in the SCS in NLOM. In addition, a $\frac{1}{8}$° global version of NLOM that includes the Sunda Shelf/Java Sea and can accurately resolve the narrow Karimata Strait has shown the net southward transport to be small (0.25 ± 0.25 Sv). The mean transport across Sunda Shelf in global NLOM is not much different from the mean 0.6 Sv estimate by Wyrtki (1961), but the model variability is more than an order of magnitude smaller than Wyrtki's seasonal estimates (summer: 3.0 Sv, winter: 4.5 Sv). Estimating the cross-sectional area of the choke point as 28 km wide by 25 m deep yields cross-sectional average velocities of 0.85, 4.3, and 6.4 m s^{-1} respectively for the mean, summer, and winter transport estimates of Wyrtki (1961). These seasonal values are unrealistically high. Global NLOM values are more realistic and yield average velocities of 0.36 ± 0.36 m s^{-1} using the same cross-sectional area defined above.

The Hellerman and Rosenstein (1983, hereafter HR) monthly mean wind stress climatology is used to spin up the model to statistical equilibrium. From this spinup model, four different initial states (each one year apart) are used as the restart conditions for the interannually wind-forced experiments. Since these experiments differ only in the initial state, any differences between them can be attributed to nondeterministic differences in both the initial conditions and the evolution of the simulations. Thus, we can use these simulations to differentiate deterministic variability in response to atmospheric forcing versus nondeterministic variability due to flow instabilities. The spinup experiment exhibits a large degree of variation in the Kuroshio intrusion, even though it is forced with monthly climatological winds. (Section 3 describes a quantitative measure of Kuroshio penetration and, for reference, the four initial states have penetration values of −1.1, 6.5, 8.7, and 15.8 cm.) This provides one of the first insights into the nondeterministic nature of the system.

Interannual forcing is by European Centre for Medium-Range Weather Forecasts [ECMWF (1995)] 1000-hectopascal (hPa) winds, and in all cases the temporal mean is replaced by the annual mean from HR as discussed in Metzger et al. (1992). This interannual forcing is referred to as an ECMWF/HR hybrid. The magnitude (but not direction) of the ECMWF winds is modified to account for the 1000-hPa level not always being at the surface (Hundermark et al. 1999). The winds are converted to a stress using the density of air (ρ_{air}) = 1.2 kg m^{-3} and a constant drag coefficient (c_d) = 1.5 × 10^{-3}. The

model is forced using 1979–93 ECMWF reanalysis 6-hourly data (Gibson et al. 1997) and then continued using 1994–97 ECMWF archived operational 12-hourly winds. The reanalysis winds have the advantage of using a constant data assimilation and atmospheric forecast model and, thus, are unaffected by product upgrades. The switch in ECMWF products across the 1993/1994 time boundary was investigated to make sure no large-scale response might be introduced into the ocean model. Pacific basin energy levels of the two wind products showed no significant change between the reanalysis/operational (Re/Op) time frames. This was not the case when the ECMWF 10-m winds were examined, hence the decision to use the 1000-hPa product. Smaller-scale differences between the two products are discussed in section 5.

b. NLOM results

1) ANNUAL SSH MEAN AND VARIABILITY

Long-term means were calculated for each of the four interannually forced experiments. At this timescale, differences were minor between the realizations. Figure 2a ⚬ shows the combined four-experiment mean SSH and upper-layer currents and can be compared to Plate 1 of MH (which shows four simulations forced by HR monthly winds). The results from the combined experiment mean are very similar to the MH results, so this leads to confidence in using the ECMWF/HR hybrid wind approach. Section 2.2 of MH also went into detail comparing NLOM transport values with observational data. While similar comparisons are not reported here, the $\frac{1}{8}$° Pacific model compares favorably.

The NEC bifurcates at the Philippines coast at approximately 14°N and, as the northward flowing Kuroshio reaches Luzon Strait, one branch bypasses the strait with flow east of the Babuyan/Batan island chain. A northwestward branch enters Luzon Strait through the Balingtang Channel, penetrates as far east as 118°E, turns anticyclonically, and exits as a northeastward flowing current through the Bashi Channel. These alternating branches of inflow/outflow agree with observational data (Nitani 1972; Huang et al. 1994), and the separation of the Kuroshio into two velocity cores as it flows past Luzon Strait is consistent with the modeling work of Chern and Wang (1998). Within the SCS basin, a well-defined cyclonic gyre exists north of 13°N except along the eastern boundary. The gyre includes a throughflow component with inflow through Luzon Strait and outflow into the Sulu Sea. A more diffuse cyclonic circulation can be seen in the southern half of the basin. In the annual mean (and the seasonal means to be shown later), the model does not produce a SCSWC as found by Guan (1978, 1985). The relatively strong southwestward flowing current seen along the boundary in the northwest SCS corresponds to the current found by Guo et al. (1985).

The 1993–97 SSH variability is shown in Fig. 2b ⚬. An area of high variability exists west of Luzon Strait at 21°N, 119°E that is associated with Kuroshio penetration and eddy shedding. The corridor of high variability extends to the southwest as the eddies propagate in that direction and the boundary current is unstable. A secondary maximum is seen off the coast of Vietnam at 12–15°N, 111°E with a weaker high variability corridor oriented southwest to northeast across the central SCS. These corridors of high SSH variability agree with contemporaneous TOPEX/Poseidon (T/P) altimeter data. The **x**'s plotted on Fig. 2b ⚬ are from Wang et al. (2000) and represent the 1993–97 mesoscale SSH variability maxima along the T/P altimeter tracks used in their study. They note decreasing variability from northeast to southwest in the northern corridor and decreasing variability from southwest to northeast in the southern corridor, as is seen in NLOM.

2) SSH ANIMATIONS

Sea surface height animations from the four realizations give an indication of the nondeterministic nature of Kuroshio penetration into the SCS. Side-by-side model comparisons rarely show the Kuroshio to be in the same configuration, suggesting that nonlinear mesoscale flow instabilities are dominant in this region. Eddy shedding from the main core of the Kuroshio is a relatively rare event during the time frame forced by ECMWF-reanalysis/HR winds (1979–93). The animations reveal instances of relatively deep intrusion and an anticyclonic eddy forming on the Pacific side of the Kuroshio within the SCS, but the eddy usually fails to separate from the main core and eventually coalesces back into the current. During the 15 year reanalysis time frame, each realization typically had only two or three eddy-shedding events (which usually did not occur in contemporaneous years). This contrasts markedly with the 4 year time frame forced by ECMWF-operational/HR winds (1994–97) in which all realizations exhibited very deep Kuroshio penetration and eddy shedding in almost all years. This difference will be discussed in more detail in section 5. The maximum model eddy diameter reaches approximately 200 km, which agrees with the observational evidence of Wang and Chern (1987a), and they have a vertical extent to the lowest model interface (1000 m), which agrees with Li et al. (1998). The animations also show other areas of favored eddy generation and propagation. In the lee of the Babuyan Island chain, anticyclonic eddies develop in August/September in about half of the model years and propagate westward. Their signature can be seen in Fig. 2b ⚬ as a tongue of slightly higher variability west of the Babuyan Islands along 19°N. The model maintains a one-gridpoint strait between Luzon Island and the shoals at 19°N, 121.5°E, and the eddies often develop when a jet of water passes through the channel. Many eddies reach the western boundary in winter and travel southwestward where they often amplify. Some propagate into the central part of the basin and merge/interact with the eddies in the interior, while others simply dissipate as they travel westward. In winter there is a direct current from the Pacific entering the SCS. As it becomes a western boundary current, eddies occasionally develop along the continental coastline and amplify as they propagate southwestward. However, these coastal eddies are more commonly generated from eddies that have either pinched off from the main core of the Kuroshio or have formed in the lee of the Babuyan Islands. In this case the eddies become finite amplitude perturbations for flow instabilities and thus amplify as they propagate west-southwestward.

3) SEASONAL MEANS

Three-month running means were combined for the four interannually forced realizations and are shown in Fig. 3 ⊙. The seasonal cycle of Kuroshio penetration agrees qualitatively with the historical surface drift data of Dale (1956) and Wyrtki (1961) and the hydrographic analysis of Shaw (1991), namely, increased intrusion in the winter months and a main core of the Kuroshio that penetrates only shallowly before retroflecting in the summer months. From November to April, a direct branch of the Kuroshio enters the SCS through Balingtang Channel. Guo et al. (1985) have named this wintertime current the SCS Branch of the Kuroshio (SCSBK), and Shaw and Chao (1994), R.-F. Li et al. (1996), and MH are numerical models that also depict it. From May to October, the Kuroshio also enters through the Balingtang Channel, but the main core retroflects on average at 120°N and exits through the Bashi Channel. The lack of the SCSBK in summer is consistent with observational studies of Xu et al. (1995) and Wang and Chern (1996). Beginning in July, a sea level dipole forms off the coast of Vietnam, peaks in strength in August, and can still be seen in September. Shaw et al. (1999) and Wu et al. (1999) present altimeter data that support such a pattern. The standard deviation of the sea surface (not shown) indicates the highest variability in the western Luzon Strait (21°N, 119°E) during the winter months associated with the deepest Kuroshio intrusion and eddy shedding.

Shaw and Chao (1994) present summer (August) to winter (February) bimonthly sea level elevation figures from their 0.4° horizontal resolution, 21-level limited-area model of the SCS forced by Hellerman and Rosenstein (1983) monthly winds and bimonthly transport estimates at the southern and northern boundaries from Wyrtki (1961). Sea level in August and October is qualitatively similar between NLOM and Shaw and Chao (1994), but different in December and February. A likely cause for some of the seasonal sea level differences is different boundary condition forcing between the models. NLOM (Fig. 3a ⊙) produces a more complete wintertime cyclonic gyre, whereas Shaw and Chao (1994) indicate that the sea level contours are open on the eastern side of the SCS. Satellite data published by Shaw et al. (1999) and Wu et al. (1999) provide an independent data source. Shaw et al. show T/P altimeter data for three days in December 1992, 1993, and 1994. Focusing on 1993, which is from a non-ENSO time frame, the satellite data indicate a basinwide cyclonic gyre system similar to the NLOM results (Fig. 3a ⊙). Additionally, the T/P data suggest that it is a two-gyre system with one center near 17°N, 117°E and one in the southern basin near 11°N, 112°E. The 1992 and 1994 data indicate weaker basinwide cyclonic gyres than in 1993, and Shaw et al. (1999) attribute this to weaker SCS circulation during ENSO events. Wu et al. (1999) use the same numerical model as Shaw and Chao (1994) but force it with NCEP/NCAR daily winds beginning in 1992. Their control run for December 1993 produces a very complete cyclonic gyre (their Fig. 3f ⊙) that is even more pronounced when they assimilate the T/P altimeter data (their Fig. 4f ⊙).

Figure 4 ⊙ is identical to Fig. 3 ⊙ except that it shows seasonal mean upper-layer currents and it is more informative in depicting the surface (non-Ekman) circulation of the SCS. It can be compared against Figure 10 ⊙ in Qu et al. (2000), which shows the seasonal variation of geostrophic velocity at 100 m. While differences exist between the modeled and observed circulation patterns, NLOM qualitatively agrees with these seasonal data. In all seasons, a southwestward current exists in NLOM along the continental coastline in the northwest SCS. This current is much broader in the winter months and is only a narrow (<1°) boundary current in July (Fig. 4c ⊙). Qu et al. (2000) point out that, despite considerable variability, a westward flow is seen during all seasons of the year. From late spring to early fall, their data suggest that the flow is narrowly confined in the continental slope south of China but does not always follow the western boundary. In NLOM, a basinwide cyclonic gyre exists in the SCS from November to February, with a stronger closed cyclonic gyre in January (Fig. 4a ⊙) centered at 8.5°N, 111°E. Fang et al. (1998) refer to this as the SCS Southern Cyclonic Gyre and include figures from Xu et al. (1982) and Fang et al. (1997) that observationally locate this wintertime gyre at 6.5°N, 109.5°E. NLOM's displacement of this gyre to the northeast may be due to the closed boundary at the Sunda Shelf or to the spatial scales resolved by the wind forcing. Shaw et al. (1999) indicate the importance of the wind stress curl in setting up the sea level in the southern basin. Adequate resolution of the wind forcing is therefore important and will be discussed later. NLOM also reproduces the wintertime north-northeastward Natuna Off-Shelf Current near 6°N, 112°E (Fang et al. 1997). The circulation in the southern SCS turns anticyclonic in summer (Fig. 4c ⊙), which again agrees with Xu et al. (1982) and Fang et al. (1997). Likewise, the Southeast Vietnam Off-Shore Current seen in these observational studies at 11°N shows up well in the modeled output.

4) LUZON STRAIT TRANSPORT

Over 1979–97, the model produces a net Luzon Strait transport (sum across all six layers) of 1.8 ± 1.0 Sv from the Pacific Ocean to the SCS. Qu (2000) used historical temperature profiles combined with climatological *T/S* relationships to obtain a Luzon Strait transport of 3.0 Sv, and Qu et al. (2000) employed the modified "island rule" to estimate the transport at 4.2 Sv. The latter study suggests that the Luzon Strait transport is a result of the counterbalance between the large-scale forcing in the Pacific Ocean and the frictional effect along the western coast of the Philippines. Because of this, they indicate that, in order to produce a reasonable estimate of Kuroshio intrusion into the SCS, the model domain must extend southward to the southern tip of the Philippines and eastward to the western coast of America. The spatial resolution must also be adequate enough to resolve most of the narrow passages that connect the SCS with the Pacific and Indian Oceans. These criteria are met with the version of NLOM used here.

Figure 5a ⊙ depicts the annual average Luzon Strait transport for the four realizations plus the combined experiment average. Relatively large interannual variations are seen from 1984 to 1990 with a trend toward higher SCS inflow transport. The net flow through Luzon Strait is always directed into the SCS with the exception of two realizations in 1984. Layer by layer, the annual mean indicates Pacific to SCS inflow in all layers, but it is very weak (<0.1 Sv) in the lowest three. Interannually, the upper layer exhibits inflow in all years, as do layers 2 and 3 with the exception of 1982–84. This contrasts with the bottom three layers that switch between inflow and outflow with an approximate 3–4 yr cycle. Using hydrographic data, Chen and Wang (1998) found intermediate water outflow in all seasons between 350 and 1350 m. Note that the total transport across the ECMWF Re/Op time boundary does not change significantly either. Metzger and Hurlburt suggests that, from a mass balance point of view, the mean Luzon Strait transport is actually an extension of the northern tropical gyre.

Thus, the wind forcing that controls the strength of this gyre appears relatively consistent for both atmospheric products that forced NLOM. Despite the large interannual variability, the net transport is very deterministic between the realizations at the yearly mean scale. Correlations are ≥0.97. Layer by layer, this determinism generally holds, as correlations are typically >0.9 for the upper four layers and >0.8 for the abyssal layer; layer 5 shows the most nondeterminism. Finally, the abyssal layer is generally in negative phase with the upper five layers.

Within the model, the inflow of Kuroshio waters into the SCS is confined between the straits north of Luzon and the northernmost Batan Islands. On average, the inflow is approximately 16 Sv summed over all six layers, but it is concentrated (>80%) within the top three layers, which have a mean depth of 440–490 m. In the annual mean the majority of the transport within the southern inflow branch simply retroflects (approximately 85%) while the remaining portion enters the SCS via Luzon Strait (Fig. 5a ⊙⊒). The SCS outflow between the northernmost Batan Islands and Taiwan is simply the inflow minus the net Luzon Strait transport and, as would be expected, it is highly correlated with the inflow ($r = -0.83$). The majority of the outflow transport is retroflected inflow, but a portion of the volume transport is due to an emptying of the SCS basin from seasonally stored water.

At the seasonal timescale, the southern Luzon Strait inflow transport is essentially constant in the upper three model layers. This contrasts with the upper-layer net (Pacific to SCS) Luzon Strait and northern Luzon Strait outflow transports. In winter, the net (northern branch) Luzon Strait transport is at maximum inflow (minimum outflow), but reverses to weak outflow (maximum outflow) in the summer. Because of the nearly constant southern inflow, the net Luzon Strait and northern outflow branches have a very high correlation, $r = 0.99$. The upper-layer northern outflow branch (and, hence, the net Luzon Strait transport) clearly responds to the seasonal northeast–southwest monsoon as depicted in Fig. 5b ⊙⊒. Significant at the 99% confidence interval, the correlation of the outflow transport with the ECMWF zonal and meridional wind stress and the wind stress magnitude is 0.95, 0.95, and −0.88, respectively.

The relationship between interannual variability in the northern branch transport and interannual variability in the northeast–southwest monsoon was investigated by computing a June–July–August (JJA) and a November–December–January (NDJ) average of the ECMWF winds and Luzon Strait transports for each year 1979–96. These 3-month bins represent the height of the southwest and northeast monsoons, respectively. For the summer season (JJA), the southern inflow, northern outflow, and net Luzon Strait transport showed similarly moderate correlations with the zonal wind stress component (0.71, −0.67, and 0.59, respectively), but the correlations were much lower for the meridional component and the wind stress magnitude. For the winter season (NDJ), no moderate correlation was found between the winds and the Luzon Strait transport. It is unclear why moderate correlations were found only for the summer zonal wind stress.

3. A quantitative measure of Kuroshio penetration

In order to better link causal effects to Kuroshio penetration, a quantitative measure of the Kuroshio intrusion was developed for the yearly mean timescale. Figure 6 ⊙⊒ shows the combined experiment long-term mean SSH for the Luzon Strait region. The difference between the areal average SSH of the diagonal box centered along the penetrating ridge and the average for the northern box in the southern Taiwan Strait comprises this quantitative measure. SSH in the northern box shows relatively low variability, while the SSH over the diagonal box provides a good measure of how deep the ridge penetrates into the basin. The difference then, allows for a quantitative comparison between the simulations.

Figure 7 ⊙⊒ depicts the Kuroshio intrusion (based on 1-yr annual mean SSH) as a function of time for the four interannually forced realizations plus the combined experiment average. The simulations show general agreement in the intradecadal variability. Moderate penetration (subjectively defined as SSH differences between 3 and 8 cm) exists in 1979. This gradually weakens to shallow penetration (SSH differences <3 cm) between approximately 1983 and 1988 and then builds to deep penetration (SSH differences >8 cm) after about 1993. Despite the general agreement, there is a lot of interexperiment variability, which provides some insight into the nondeterministic nature of Kuroshio intrusion. Correlations between the curves ranged from 0.42 to 0.77 over the 1979–97 time period, but the deep penetration during the ECMWF operational wind period appears related to differences in the annual mean wind curl compared to the reanalysis period. This will be discussed in more detail in section 5. The correlations computed just over the reanalysis time period are very low, <0.42, with the exception of one experiment pair.

The quantitative measure of Kuroshio penetration appears to work well for the annual timescale, but breaks down when looking at the seasonal cycle. The technique indicates maximum Kuroshio intrusion during the summer months with weakest intrusion in the winter (not shown), while the monthly mean SSH indicates just the opposite (note the 30-cm isoline in Fig. 3 ⊙⊒). This occurs because wintertime storage of upper ocean water within the SCS affects the measure. That upper-layer water stored in the SCS in winter exits through Luzon Strait in the summer, as seen in Fig. 3c ⊙⊒, consistent with the observational study by Chu (1972). Note how the SSH contours emanate from the central SCS basin and exit in the northern half of the strait. In doing so they add to the areal average of diagonal box and bias the results.

4. Nondeterminism in the SCS

a. Kuroshio intrusion into the SCS

Metzger et al. (1994) developed a technique to separate the variability of a given model variable into two components, one caused by direct atmospheric forcing (deterministic) and the other caused by mesoscale flow instabilities (nondeterministic). This can be applied here and is possible because all the simulations are identical, except for their initial state. Spatial maps can then be created to determine the relative importance of the two anomaly generation mechanisms.

Using SSH as an example, the technique is as follows. First, the long-term mean SSH is computed for each experiment and averaged over the four realizations (Fig. 2a ⊙▬). This is then subtracted from each record (3.05 days apart) of the individual simulations to form four time series of SSH anomaly fields (η). At each grid point, the temporally corresponding records of the four realizations are averaged ($\overline{\eta}$) and deviations ($\eta' = \eta - \overline{\eta}$) computed about the combined experiment mean. These are then combined and averaged as follows:

$$\overline{\eta^2} = \overline{\eta}^2 + \overline{\eta'^2},$$

where the bar is the average of the four realizations. Except for the removal of the combined temporal mean, no averaging through time is required to obtain these results. However, the most meaningful results are obtained by temporally averaging the above results over the same period as the temporal mean removed. That way the temporal average of the deterministic anomalies is zero. The left-hand side represents the total SSH variability and the right-hand side represents the SSH variability due to atmospheric forcing plus the variability due to flow instabilities, assuming $\overline{\eta}$ is accurately defined by a large number of realizations. After dividing the equation by the total SSH variability ($\overline{\eta^2}$), maps can be produced that show the fraction of the SSH variability due to either atmospheric forcing or flow instabilities, respectively.

With a small number of model realizations the flow instabilities component is underestimated and the wind forcing component is overestimated. This is especially true for areas dominated by mesoscale flow instabilities such as the Kuroshio Extension region. Consider the case where the true deterministic component is zero. Generally the average over the realizations will not be zero, but closer to zero as the number of realizations increases. The fraction of variability was computed for two, three, and four realizations and with the addition of each successive model run, the fraction due to flow instabilities grew. While convergence has probably not been achieved for this technique, the fields nonetheless indicate regions where deterministic and nondeterministic variability are relatively important.

Figure 8 ⊙▬ shows the fractional SSH variability for the SCS region and has been broken down into two periods, 1979–93 and 1994–97, because of the different character of Kuroshio intrusion when NLOM is forced with reanalysis and operational winds, respectively. Dark blue (orange) areas are regions where SSH variations are predominantly caused by wind forcing (mesoscale flow instabilities). Most areas represent a combination of the two variability mechanisms, but relative orange maxima for both periods are seen in the vicinity of Luzon Strait, indicating that the intrusion of the Kuroshio into the SCS has a substantial nondeterministic component in its variability. The SSH variability associated with inflow in the southern half of the strait appears more deterministic than that associated with outflow in the northern half of the strait. Note also the corridor of relatively nondeterministic SSH variability leading southwestward away from the strait. This is associated with eddy development and propagation in the model. Substantial differences are also seen between the two time periods with the operational wind forcing resulting in a larger degree of nondeterminism in the vicinity of Luzon Strait and in the interior of the SCS basin. While the operational winds produce a more consistent, deep Kuroshio intrusion than the reanalysis winds, it is clear that the magnitude and spatial extent varies greatly between the realizations. The higher degree of nondeterminism in the interior of the basin also suggests that the higher resolution operational winds (more details regarding this in section 5) may be resolving smaller-scale wind features, which might in turn trigger more oceanic flow instabilities.

The fractional velocity variability is much more nondeterministic in the Luzon Strait region (not shown). The nondeterministic component accounts for >65% of the velocity variability for both the zonal and meridional components. Unlike the SSH variability, the southern half of the strait is equally as nondeterministic as the northern half.

From the preceding analysis, it appears then that Kuroshio penetration on the interannual timescale is not solely related to direct atmospheric forcing. Given that all four simulations were forced with identical winds, perturbations caused by the different initial states of each realization are introducing a nondeterministic component as a result of mesoscale flow instabilities. Modeling this region at an even higher horizontal resolution would likely increase the nondeterministic component.

Despite the large element of nondeterminism in the system, attempts were made to relate the Kuroshio intrusion to the oceanic environment. For example, is the penetration related to current transports in the vicinity of Luzon Strait? Annual mean modeled transport was determined for four sections (which comprised a box): across Luzon Strait along 120.7°E (Fig. 5a ⊙▬), east of Taiwan along 22°N, a north–south section east of Luzon Strait along 124.6°E, and east of Luzon Island along 18°N. Correlations between the quantitative measure of Kuroshio penetration (Fig. 7 ⊙▬) and the time series of annual mean transport for the four sections were low; this applied to layer by layer analysis, as well as the sum of all six model layers. For the three sections away from Luzon Strait, correlations ranged from −0.1 to −0.3. The range in correlation between the Kuroshio intrusion and Luzon Strait transport was stronger, −0.4 to −0.55, correlations significant at the 95% confidence level. However, Kuroshio transport did not affect Kuroshio penetration.

The NEC bifurcates at 14°N along the Philippines coast on average in NLOM, but interannually (seasonally) this latitude can vary by 3° (2°). (The bifurcation latitude across the four realizations is relatively deterministic and correlations between the simulations are typically >0.8.) As the bifurcation latitude shifts southward (northward), the Kuroshio transport east of Luzon increases (decreases). Corroborating the analysis above, no meaningful relationship between Kuroshio penetration and the NEC bifurcation latitude was found; correlations ranged from 0.1 to 0.5 with those correlations greater than 0.4 being statistically significant at the 90% confidence interval.

In addition, a causal relationship between the Kuroshio intrusion and the atmosphere is explored. Looking at just the

reanalysis time frame, the wind stress is averaged over a 4° × 4° box centered at 20°N, 120°E, as defined by Farris and Wimbush (1996). Neither the zonal or meridional components nor the wind stress magnitude correlate well with the measure of yearly mean Kuroshio intrusion.

b. The SCS and the western equatorial Pacific

Using the quantitative measure of Kuroshio penetration, previous analysis has indicated that the four simulations show a lot of interexperiment variability. But, is this true for regions away from Luzon Strait or for a larger subregion within the strait? This is examined by correlating yearly mean SSH anomalies over wider spatial areas. One-year means are calculated for each realization and the combined experiment long-term mean (with respect to 1979–97 and 1979–93) is subtracted to create four time series of yearly mean anomalies. The calculations are performed relative to the two long-term means because of the significant change in behavior of the Kuroshio intrusion during the ECMWF operational wind period (1994–97). Three subregions are examined: 1) the Luzon Strait region where the ridge of SSH penetrates into the SCS (20°–22.5°N, 118°–121°E), 2) the entire SCS (5°–22.5°N, 109°–121°E) region, and 3) the extreme western equatorial Pacific (0°–22.5°N, 121°–135°E). Within each subregion, experiment by experiment correlation analysis is performed over all model years to see if a degree of determinism can be found.

As expected over the Luzon Strait subregion, yearly SSH anomaly correlations between the simulations varied widely for a given year and showed large interannual variations. The median correlation over all the experiments and all years was 0.59 with respect to the 1979–97 mean, but this fell to 0.3 with respect to the 1979–93 mean. This large difference is due to the consistent, deep penetration of the Kuroshio during 1994–97, which tends to make the intrusion process appear more deterministic over this subregion.

Over the SCS subregion, there was not as much overall interexperiment variation for a given year compared to the Luzon Strait subregion, but there was still a lot of interannual variability in these correlations. Correlating the anomalies relative to the two long-term means did not produce as large a difference in the overall median correlation, which was 0.57 (0.49) relative to the 1979–97 (1979–93) mean. Thus, the SCS also exhibits a large degree of nondeterminism in the yearly mean SSH signal due to flow instabilities.

In contrast to the two subregions above, the western equatorial Pacific subregion is much more deterministic at both annual and interannual timescales. For a given year there is very little interexperiment variation of the yearly SSH anomaly correlations, and the median correlation over all experiments and years is 0.91 (relative to both long-term means). Thus, the yearly mean SSH variations in the extreme western equatorial Pacific, which are predominantly larger in scale, appear to be largely deterministic, wind-forced phenomena.

c. Intradecadal variability

After looking at the Kuroshio intrusion as a function of time (Fig. 7 ☊), there appear to be periods when the penetration is similar for several years in a row. Overall, 1983–90 are years of shallow Kuroshio penetration while 1994–97 are years of deep penetration; 1979–82 and 1991–93 are transition years between the two extremes with moderate Kuroshio intrusion. Means are created over these four time groups and anomalies of these relative to both the 1979–97 and 1979–93 combined experiment long-term means are again computed for each experiment. Correlation analysis is performed over the same three subregions defined in the previous section.

Unlike the yearly anomaly correlations, the 1983–90 and 1994–97 time group interexperiment anomaly correlations for Luzon Strait are quite high, >0.9. However, the 1979–82 and 1991–93 time groups had very weak correlations between the experiments with median correlations near zero. This suggests a certain amount of intradecadal determinism when the Kuroshio intrusion is in one of two extreme modes, either deep penetration or very shallow penetration. These results apply for anomalies relative to both long-term means.

For the SCS region, the same results apply, but the median correlations for the extrema year time groupings (0.8) are not substantially higher than the median correlation for the transitional year time groups (0.6). In the western equatorial Pacific region, correlations are greater than 0.9 for all time groups.

5. ECMWF reanalysis versus operational wind forcing

As mentioned previously, the character of the Kuroshio intrusion into the SCS is greatly different depending upon the time frame of the ECMWF forcing. During the reanalysis wind period (1979–93), deep Kuroshio penetration is a relatively rare event, but during the operational wind period (1994–97) there is a persistent deep intrusion of the Kuroshio. An initial hypothesis for the different behavior is possible strengthening of the northern tropical or subtropical gyre. Metzger and Hurlburt points out that the Luzon Strait transport is actually an extension of the northern tropical gyre. If the strength of the northern tropical gyre increases, the Luzon Strait transport should increase, while the Kuroshio transport just north of Luzon Strait would remain the same. Conversely, if the strength of the subtropical gyre increases, the Kuroshio transport just north of the Luzon Strait should increase, while the Luzon Strait transport would remain the same. No significant change in either the Luzon Strait transport (Fig. 5a ☊) or Kuroshio transport was detected across the ECMWF Re/Op time boundary, so large-scale atmospheric changes do not appear to be the cause. This is further corroborated by analyzing the atmospheric energy levels over the northern tropical and subtropical gyres (not shown). No change is detected across the ECMWF Re/Op time boundary.

The local wind stress in the SCS/Philippines region is examined next to see if it might provide insight concerning the different character of Kuroshio penetration. Atmospheric energy levels (not shown) are computed for three regions: 1) the entire Philippines/SCS (0°–30°N, 110°–135°E), 2) the Luzon Strait region and the area of strong monsoonal winds to the northeast (18°–30°N, 110°–139°E) similar to the area chosen for wind analysis in MH, and 3) a more locally confined Luzon Strait region (16°–26°N, 113°–125°E). From the mid-1980s to 1990 the two products show very consistent energy levels over all the subregions, but in 1991 a small divergence between the curves begins with the operational winds about 10% stronger. This is probably due to a change in the atmospheric model resolution, which is described later. However, this approximate 10% upward shift is still within the range of the interannual variability of the atmospheric energy levels, and thus we suggest that wind stress changes across the ECMWF Re/Op time boundary are not causing the marked shift in Kuroshio intrusion.

Then what about the wind stress curl in Luzon Strait? Yearly mean curl fields indicate a significant difference over Luzon Strait and in many other regions. Figure 9 shows yearly mean curl for 1993, the last year of overlap between the two products. The curl pattern for this year is representative of most other years in each dataset. Both products indicate negative curl in the northern half of the strait and positive curl in the southern half of the strait; yet the magnitudes differ substantially. Wind curl extrema from the operational winds are more than twice as large, and the gradient in curl is much sharper. In addition, the pattern of curl over the interior of the SCS is also quite different. So, while wind stress magnitude is fairly consistent between the two products, the distribution of curl has some substantial differences.

The ECMWF operational winds are obtained from NCAR and are named the ECMWF Tropical Ocean Global Atmosphere (TOGA) global basic surface and upper-air analyses (NCAR dataset DS111.2). Since September 1991, the operational atmospheric model running at ECMWF has had a T213 spectral resolution (0.85° along the equator). However, a spherical truncation to T63 (2.8° along the equator) is performed and then interpolation to a 2.5° Cartesian grid before distribution. In contrast, the reanalysis winds obtained through NCAR are the ECMWF reanalysis basic global upper-air dataset (DS115.1). The model resolution is spectral T106 (1.7° along the equator) with a spherical harmonic truncation to T47 (3.8° along the equator) before final interpolation to the 2.5° grid. In the interior of the SCS, the large and small scale structure of the wind curl differs. It is clear that the higher-resolution operational winds pick up more small-scale structure, in addition to producing larger extreme values. These differences appear to be related to the truncation technique employed within each dataset, but further study is needed to corroborate this.

Because of an overlap between the ECMWF operational and reanalysis winds, it is possible to investigate model sensitivity to these two wind products. Two additional experiments are integrated over 1992–93, but the ECMWF operational winds force the model. The initial states for these two simulations are the first record of 1992 from two of the simulations run with ECMWF reanalysis winds. Thus, there will be two sets of experiment twins that start from the same initial state but have different wind forcing. Figure 7 indicates a lot of interexperiment variability with regard to Kuroshio penetration in 1992–93, with experiment 1 showing moderately deep intrusion and experiment 2 showing shallow intrusion. These two extreme cases are chosen as the initial states for the new experiments described above.

Figure 10 shows the 1993 annual mean SSH for the two twin experiments and the plus signs on Fig. 7 indicate the quantitative measure of Kuroshio intrusion for the two new experiments. In both cases, the experiments forced by ECMWF operational winds exhibit deeper Kuroshio penetration than its twin forced with ECMWF reanalysis winds. This suggests that the larger negative curl over the northern Luzon Strait creates more Ekman pumping, which causes the thermocline to deepen and in turn leads to greater intrusion of the Kuroshio. Given this hypothesis, one might expect wind curl over Luzon Strait to be highly correlated with Kuroshio penetration, but this is not the case. Over the reanalysis period, the correlation coefficient between the Kuroshio intrusion and wind curl (averaged over the region of the mean penetrating Kuroshio) is small ($r = -0.25$). This again highlights the nondeterministic nature of the Kuroshio intrusion into the SCS. However, the results imply that large changes in wind stress curl magnitudes and patterns over Luzon Strait do significantly affect the modeled Kuroshio pathway and its interaction with the SCS. The operational products produce curl maxima that are more than twice as large as the reanalysis products, and this is greater than the interannual variability of the wind stress curl over this region.

Note also in Fig. 10 the differences in the circulation in the interior of the SCS brought about by wind stress curl changes. Both simulations forced with ECMWF reanalysis winds (Figs. 10a,c) produce a single, northern basin cyclonic gyre while the ECMWF operational wind forced experiments (Figs. 10b,d) have two distinct gyres, one northeast of Vietnam near 15°N, 111°E and one west of Luzon near 17°N, 117°E. Thus, the ocean model is responding to the smaller spatial scales in the ECMWF operational wind curl. It appears then, to most accurately model the SCS region, numerical modelers would be wise to choose a wind-forcing dataset with the highest possible horizontal resolution. These products are available at NCAR and are the ECMWF reanalysis advanced global dataset (DS115.4) or the ECMWF TOGA global advanced operational spectral analyses (DS111.0). Both are output on a T106 spectral grid (which is the full model resolution during the reanalysis, but a truncated resolution of the operational winds). However, these products are more expensive and have substantially increased storage requirements compared to the products distributed on the 2.5° Cartesian grid.

6. Summary

The results presented here suggest a large degree of nondeterminism regarding the Kuroshio intrusion into the SCS. Four numerical experiments were forced with 1979–97 ECMWF reanalysis and operational winds and only differ in their initial state. Because the evolution of the Kuroshio's interaction with the SCS can be quite different between all four realizations, mesoscale flow instabilities must be contributing to the nondeterminism of the system. One would expect these flow

instabilities to dominate even more in the real ocean and at model resolutions higher than the $\frac{1}{8}°$ used here. Thus, the results suggest that on the yearly mean timescale, Kuroshio intrusion does not appear to be a wind-forced, deterministic event.

A description of the long-term mean SSH is given along with a discussion of its time evolution. In the Luzon Strait region, contemporaneous interexperiment comparisons of instantaneous SSH rarely show the Kuroshio to be in the same configuration. Eddy generation in Luzon Strait can occur when the Kuroshio intrudes deeply into the SCS basin and pinches off a vortex. Deep penetration and eddy shedding are relatively rare events, occurring only two or three times during the ECMWF reanalysis forcing (1979–93) but are persistent features in almost all years for the ECMWF operational winds (1994–97). In August/September, a secondary area of favored eddy generation exists in the lee of the Babuyan Island chain.

In order to quantify the Kuroshio intrusion into the SCS, a measure was developed for the yearly mean timescale that examined the difference between the areal average SSH in the southern Taiwan Strait and along the penetrating SSH ridge axis. This difference allowed quantitative intercomparison of the simulations and investigation of interannual variability. It showed general interexperiment agreement for the intradecadal variations, but a lot of interexperiment variability for any given year. Kuroshio intrusion correlations between experiments were low for the interannual time series.

Using this intrusion measure, hypotheses relating Kuroshio penetration to the oceanographic environment or atmospheric forcing were also investigated. The results indicate that the Kuroshio intrusion is not a function of the oceanic transport through Luzon Strait nor of the surrounding Pacific Ocean waters, including Kuroshio transport north or south of Luzon Strait. Yearly mean transports from transects across Luzon Strait, east of Luzon, east of Taiwan, and a north–south section east of Luzon Strait along 124.6°E did not strongly correlate with the Kuroshio intrusion. The NEC bifurcation latitude was also examined since, as it shifts southward (northward), the Kuroshio transport east of Luzon increases (decreases). Corroborating the previous analysis, no meaningful relationship was found with Kuroshio penetration.

In addition, interannual variations of the wind in the vicinity of Luzon Strait were studied. No tangible relationship could be found that linked interannual variability of yearly mean Kuroshio intrusion or monsoon season mean Luzon Strait transport with corresponding zonal or meridional wind components, wind stress magnitude, or wind stress curl. However, there was a close relationship between the mean seasonal cycles of the Luzon Strait transport and the northeast–southwest monsoon.

As mentioned, the quantitative measure of the Kuroshio intrusion showed substantial interexperiment interannual variability. Wider spatial areas in and away from Luzon Strait were examined to see if the same was true. Yearly mean SSH anomalies from each experiment were intercorrelated for a larger Luzon Strait subregion, the SCS basin subregion and the extreme western equatorial Pacific Ocean. The interexperiment correlations for all the ECMWF reanalysis forced years produced median correlations of 0.3, 0.49, and 0.91 for the three subregions, respectively. Thus the SCS basin also exhibits a large degree of nondeterminism in the yearly mean SSH signal due to flow instabilities, but the western equatorial Pacific appears to be a region governed by largely deterministic wind-forced phenomena.

Much greater Kuroshio penetration was found after switching to archived operational winds at the end of the ECMWF reanalysis. An initial hypothesis for the change in behavior was possible strengthening of the northern tropical or subtropical gyres. Since the Luzon Strait transport is actually an extension of the northern tropical gyre, the transport should increase with an increase in the strength of this tropical Pacific gyre. Likewise, increases in subtropical gyre strength should produce an increase in transport just north of Luzon Strait. No significant change in these transports was detected across the ECMWF reanalysis/operational time boundary, so large-scale atmospheric changes do not appear to be the cause.

The local wind stress in the Luzon Strait/SCS region was also studied to provide insight into the different character of the Kuroshio intrusion. No significant change across the reanalysis/operational time boundary was found for the wind stress. However, yearly mean wind stress curl fields revealed marked differences. Both reanalysis and operational products produce negative curl in the northern Luzon Strait and positive curl in the southern strait, but the magnitudes differ substantially. Wind curl extrema from the operational winds are more than twice as large, and the gradient in curl is much sharper. The pattern of curl over the interior of the SCS is also quite different. The net effect in the model is larger Ekman pumping, a deepening of the thermocline, and in turn greater westward Kuroshio penetration into the SCS during the 1994–97 ECMWF operational forcing time frame. There are also substantial changes within the SCS basin.

While the simulated Kuroshio intrusion clearly responds differently to the ECMWF operational and reanalysis winds, neither period exhibits much determinism in the variability. Deep Kuroshio intrusion is sporadic during the reanalysis wind forcing, whereas the operational winds produce a consistent, deep penetration. It might appear that the operational winds produce a more deterministic response, but the strength of the deep intrusion during 1994–97 is highly variable (Figs. 7 and 8b ⊙=). In fact, the interexperiment root mean square of the quantitative measure of Kuroshio intrusion calculated over the operational wind forcing period (6.4 cm) is higher than that of the reanalysis wind period (5.0 cm). Thus, the determinism does not seem to be dependent on the flow regime.

The difference in the curl distribution is probably related to the manner in which the two atmospheric products have been truncated on their spectral grid before distribution on the 2.5° grid. Investigation of this topic requires further study and is beyond the scope of this paper, but as ocean model resolution becomes finer, the resolution of the atmospheric forcing driving these models must also increase in order to represent smaller spatial scales.

REFERENCES

Chen C.-T., and S.-L. Wang, 1998: Influence of intermediate water in the western Okinawa Trough by the outflow from the South China Sea. *J. Geophys. Res*, **103**, 12 683–12 688.

Chern C.-S., and J. Wang, 1998: A numerical study of the summertime flow around the Luzon Strait. *J. Oceanogr*, **54**, 53–64. Find this article online

Chu T.-Y., 1972: A study on the water exchange between the Pacific Ocean and the South China Sea. *Acta Oceanogr. Taiwan*, **2**, 11–24. Find this article online

Chuang W. S., 1986: A note on the driving mechanism of current in the Taiwan Strait. *J. Oceanogr. Soc. Japan*, **42**, 355–361. Find this article online

Dale W. L., 1956: Wind and drift currents in the South China Sea. *Malays. J. Trop. Geogr*, **8**, 1–31. Find this article online

ECMWF,, 1995: User guide to ECMWF products. Meteorological Bulletin M3.2, 71 pp.

Fang G., W. Fang, Y. Fang, and K. Wang, 1998: A survey of studies on the South China Sea upper ocean circulation. *Acta Oceanogr. Taiwan*, **37**, 1–16. Find this article online

Fang W., Z. Guo, and U. Huang, 1997: Observation and study on the circulation in the southern South China Sea (in Chinese). *Chin. Sci. Bull*, **42**, 2264–2271. Find this article online

Farris A., and M. Wimbush, 1996: Wind-induced Kuroshio intrusion into the South China Sea. *J. Oceanogr*, **52**, 771–784. Find this article online

Gibson J. K., P. Kållberg, S. Uppala, A. Hernandez, A. Nomura, and E. Serrano, 1997: ERA description. ECMWF Re-Analysis Project Report Series, No. 1, ECMWF, 72 pp.

Guan B., 1978: New evidence of the South China Sea Warm Current (in Chinese). *Ocean Sci*, 100–103.

—— ,1985: Some features of the temporal and spatial distributions of the "counter-wind" current in the northern South China Sea in winter (in Chinese with English abstract). *Oceanol. Limnol. Sin*, **16**, 429–438>, (6),. Find this article online

Guo Z., and W. Fang, 1988: The Kuroshio in Luzon Strait and its transport during September 1985, (in Chinese with English abstract). *Trop. Oceanol*, **7**, 13–19. Find this article online

—— ,T. Yang, and D. Qiu, 1985: The South China Sea Warm Current and the southwestward current on its right side in winter (in Chinese with English abstract). *Trop. Oceanol*, **4**, 1–9, (1),. Find this article online

Hellerman S., and M. Rosenstein, 1983: Normal monthly wind stress over the World Ocean with error estimates. *J. Phys. Oceanogr*, **13**, 1093–1104. Find this article online

Huang Q., W. Wang, Y. Li, and C. Li, 1994: Current characteristics of the South China Sea. *Oceanology of China Seas,* D. Zhou, Y.-B. Liang, and C.-K. Zeng, Eds., Vol. 1, Kluwer Academic, 39–47.

Hundermark B. W., H. E. Hurlburt, E. J. Metzger, and J. F. Shriver, 1999: A comparison of wind stresses derived from archived operational ECMWF 1000 mb winds and FSU pseudo stresses over the tropical Pacific Ocean, 1981–93. Naval Research Laboratory Rep. NRL/FR/7320-99-9643, Stennis Space Center, MS, 40 pp.

Hurlburt H. E., and J. D. Thompson, 1980: A numerical study of Loop Current intrusions and eddy shedding. *J. Phys. Oceanogr*, **10**, 1611–1651. Find this article online

—— ,and —— ,1982: The dynamics of the Loop Current and shed eddies in a numerical model of the Gulf of Mexico. *Hydrodynamics of Semi-Enclosed Seas,* J. C. J. Nihoul, Ed., Elsevier Scientific, 243–298.

Levitus S., and T. P. Boyer, 1994: *World Ocean Atlas1994*. Vol. 4: *Temperature.* NOAA Atlas NESDIS, 117 pp.

—— ,R. Burgett, and T. P. Boyer, 1994: *World Ocean Atlas 1994,* Vol.3: *Salinity* NOAA Atlas NESDIS, 99 pp.

Li L., W. D. Nowlin, and J. Su, 1998: Anticyclonic rings from the Kuroshio in the South China Sea. *Deep-Sea Res. Part I*, **45**, 1469–1482. Find this article online

Li R.-F., Q.-C. Zeng, Z.-J. Gan, and W.-Z. Wang, 1993: Numerical simulation of the South China Sea Warm Current and the Taiwan Strait

flow in winter. *Prog. Natl. Sci*, **3**, 123–129.

— , D.-J. Guo, and Q.-C. Zeng, 1996: Numerical simulation of interrelation between the Kuroshio and the current of the northern South China Sea. *Prog. Natl. Sci*, **6**, 325–332, (3),.

Li W., Q. Liu, and S.-P. Cheng, 1996: The effect of a break in western boundary on the Western Boundary Current. *Acta Oceanogr. Taiwan*, **35**, 141–153. Find this article online

Metzger E. J., and H. E. Hurlburt, 1996: Coupled dynamics of the South China Sea, the Sulu Sea and the Pacific Ocean. *J. Geophys. Res*, **101**, 12 331–12 352.

— , — , J. C. Kindle, Z. Sirkes, and J. M. Pringle, 1992: Hindcasting of wind-driven anomalies using a reduced gravity global ocean model. *J. Mar. Technol. Soc*, **26**, 23–32, (2),.

— , — , G. A. Jacobs, and J. C. Kindle, 1994: Hindcasting wind-driven anomalies using reduced gravity global ocean models with ½° and ¼° resolution. Naval Research Laboratory Rep. NRL/FR/7323-93-9444, Stennis Space Center, MS, 21 pp.

Moore D. R., and A. J. Wallcraft, 1998: Formulation of the NRL Layered Ocean Model in spherical coordinates. Naval Research Laboratory Rep. NRL/CR/7323-96-0005, Stennis Space Center, MS, 24 pp.

Nitani H., 1972: Beginning of the Kuroshio. *Kuroshio: Physical Aspects of the Japan Current,* H. Stommel and K. Yoshida, Eds., University of Washington Press, 129–163.

NOAA,, 1986: ETOP05 digital relief of the surface of the Earth. Data Announcement 86-MGG-07, National Geophysical Data Center, Boulder, CO, 1 p.

Qu T., 2000: Upper layer circulation in the South China Sea. *J. Phys. Oceanogr*, **30**, 1450–1460. Find this article online

— , H. Mitsudera, and T. Yamagata, 1998: On the western boundary currents in the Philippine Sea. *J. Geophys. Res*, **103**, 7537–7548.

— , — , and — , 2000: Intrusion of the North Pacific waters into the South China Sea. *J. Geophys. Res*, **105**, 6415–6424.

Shaw P.-T., 1989: The intrusion of water masses into the sea southwest of Taiwan. *J. Geophys. Res*, **94**, 18 213–18 226.

— , 1991: The seasonal variation of the intrusion of the Philippine sea water into the South China Sea. *J. Geophys. Res*, **96**, 821–827.

— , and S.-Y. Chao, 1994: Surface circulation in the South China Sea. *Deep-Sea Res. Part I*, **41**, 1663–1683. Find this article online

— , — , and L.-L. Fu, 1999: Sea surface height variations in the South China Sea from satellite altimetry. *Oceanol. Acta*, **22**, 1–17, (1),. Find this article online

Shriver J. F., and H. E. Hurlburt, 1997: The contribution of the global thermohaline circulation to the Pacific to Indian Ocean throughflow via Indonesia. *J. Geophys. Res*, **102**, 5491–5511.

Wallcraft A. J., 1991: The Navy Layered Ocean Model user's guide. NOARL Rep. 35, Naval Research Laboratory, Stennis Space Center, MS, 21 pp.

— , and D. R. Moore, 1997: The NRL Layered Ocean Model. *Parallel Comput*, **23**, 2227–2242. Find this article online

Wang J., and C.-S. Chern, 1987a: The warm-core eddy in the northern South China Sea, I. Preliminary observations on the warm-core eddy. *Acta Oceanogr. Taiwan*, **18**, 92–103. Find this article online

— , and — , 1987b: The warm-core eddy in the northern South China Sea, II. A simple mechanism for the establishment and development of the warm-core eddy. *Acta Oceanogr. Taiwan*, **18**, 104–113. Find this article online

— , and — , 1996: Some aspects on the circulation in the northern South China Sea. *La Mer*, **34**, 246–257. Find this article online

Wang L., C. J. Koblinsky, and S. Howden, 2000: Mesoscale variability in the South China Sea from TOPEX/Poseidon altimetry data. *Deep-Sea Res. Part I*, **47**, 681–708. Find this article online

Wu C.-R., P.-T. Shaw, and S.-Y. Chao, 1999: Assimilating altimetric data into a South China Sea model. *J. Geophys. Res*, **104**, 29 987–30 005.

Wyrtki K., 1961: Physical oceanography of the southeast Asian waters. NAGA Rep. 2, Scripps Institute of Oceanography, La Jolla, CA, 195 pp.

Xu J., J. Su, and D. Qiu, 1995: Hydrographic analysis on the intruding of Kuroshio water into the South China Sea. *Proc. Symp. of Marine Sciences in the Taiwan Strait and its Adjacent Waters,* Guangzhou, China, Chinese National Sciences Foundation, 30–44.

Xu X., Q. Zhang, and H. Chen, 1982: The general descriptions of the horizontal circulation in the South China Sea (in Chinese with English abstract). *Proc. Symp. of the Chinese Society of Marine Hydrology and Meteorology,* Chinese Society of Oceanology and Limnology, 119–127.

Zhao B., and and Fang G., 1991: Estimation of water volume transports through the main straits of the East China Sea. *Acta Oceanol. Sin*,

Tables

TABLE 1. Unvaried model parameters

Parameter	Value	Definition
A_H	100 m² s⁻¹	Coefficient of horizontal eddy viscosity
C_b	2×10^{-3}	Bottom drag coefficient
C_k	0	kth interfacial stress coefficient
C_M	1	Coefficient of additional interfacial friction associated with entrainment
g	9.8 m s⁻²	Acceleration due to gravity
H_k	80/140/160/245 375/bottom	kth layer thickness at rest (in meters)
h_k^+	50 m ($k = 1$) 40 m ($k = 2$–6)	Thickness of layer k at which entrainment starts
h_k^-		Thickness of layer k at which noncompensating detrainment starts; not used by setting to a large value
K_H	300 m² s⁻¹	Coefficient of horizontal density diffusivity
K_{H_k}	0	Coefficient of biharmonic horizontal density diffusivity
$\hat{K}_{H_k}$	0	Coefficient of biharmonic horizontal layer of thickness diffusion
$\rho_{k+1} - \rho_k$	1.86/1.38/0.56/0.38/0.43	Stratification at rest between layer k and $k + 1$ in kg m⁻³
Q	0	Total surface heat flux
$\bar{\omega}_k$	0.04 m s⁻¹	kth interface reference vertical mixing velocity

Click on thumbnail for full-sized image.

Figures

Click on thumbnail for full-sized image.

FIG. 1. Geometry of the South China Sea region plotted on the $\frac{1}{8}°$ NRL Layered Ocean Model grid. The model land–sea boundary is the 200-m isobath, except for Taiwan Strait and the two interior Philippines passages
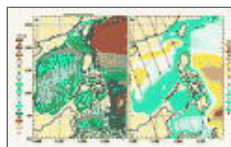
Click on thumbnail for full-sized image.

FIG. 2. (a) Mean SSH and upper-layer currents from the $\frac{1}{8}°$, 6-layer finite depth thermodynamic model of the Pacific Ocean north of 20°S with realistic bottom topography. Only the SCS subregion is shown. The mean covers the 1979–97 time frame and is an average of four model realizations, which only differ in their initial state. The simulations were forced with the ECMWF/HR hybrid winds (see text for details). The SSH contour interval is 5 cm and the reference vector at the top is 1 m s⁻¹. (b) Rms SSH over 1993–97 from the same four simulations with a contour interval of 2 cm. The **x**'s represent the mesoscale SSH variability maxima along TOPEX/Poseidon altimeter tracks over the same time period as determined by Wang et al. (2000)
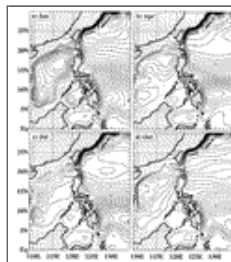
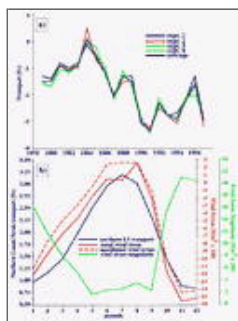Click on thumbnail for full-sized image.

FIG. 3. The combined experiment 3-month running mean SSH from the four NLOM realizations centered over (a) Jan, (b) Apr, (c) Jul, and (d) Oct. The contour interval is 2.5 cm
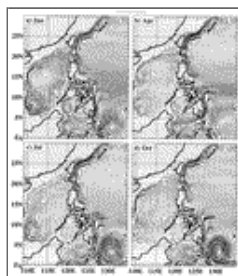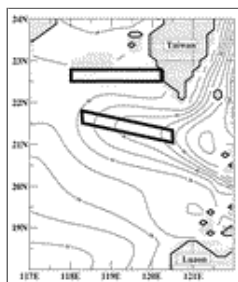

Click on thumbnail for full-sized image.

FIG. 4. As in Fig. 3 ⊙▬ except for upper-layer current vectors. The reference vector (at the top) is 1 m s^{-1}

Click on thumbnail for full-sized image.

FIG. 5. (a) Model transport (in Sv) vs time through Luzon Strait (between Taiwan and Luzon along 120.7°E) for the four $\frac{1}{8}°$ NLOM realizations plus their average. Data points are means for each model year and the sum of all six model layers. (b) Monthly upper-layer model transport (blue) for the northern Luzon Strait outflow (i.e., between Taiwan and the northernmost Batan Islands), zonal (red solid) and meridional (red dashed) wind stress, and wind stress magnitude (green). The transport (in Sv) is an average of the four $\frac{1}{8}°$ NLOM realizations, and the ECMWF winds are averaged over a 4° × 4° box centered at 20°N, 120°E as defined by Farris and Wimbush (1996) with units of N m^{-2} × 100

Click on thumbnail for full-sized image.

FIG. 6. The combined experiment 1979–97 mean SSH for the Luzon Strait region. The contour interval is 2.5 cm. The two boxes define the locations over which the areal average SSH is calculated and then differenced to produce a quantitative measure of Kuroshio penetration into the SCS
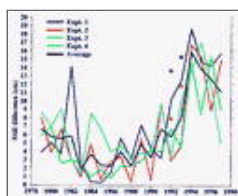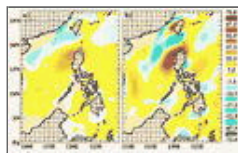

Click on thumbnail for full-sized image.

FIG. 7. Kuroshio penetration vs time for the four NLOM realizations plus their average. Penetration is defined as the SSH difference (in cm) of the areal average of the two boxes defined in Fig. 6 ⊙▬. Larger SSH differences indicate deeper Kuroshio intrusion. The plus signs at 1992 and 1993 measure Kuroshio intrusion from two additional experiments forced by the ECMWF operational winds that overlap the reanalysis winds in time; the blue (red) plus signs are for the twin to experiment 1 (2)

FIG. 8. The fraction of the modeled SSH variability for (a) 1979–93 and (b) 1994–97 from the four $\frac{1}{8}°$ NLOM simulations caused by direct wind forcing (predominantly deterministic: blue areas) and by flow instabilities (predominantly nondeterministic: orange/red areas). The field has been normalized by the total SSH variability at each grid point. The velocity field (not shown) is more nondeterministic than the SSH field. The combined experiment temporal means, used to calculate anomalies, were calculated separately for the time periods 1979–93 and 1994–97. That way the temporal means of the deterministic anomalies were zero over the time frame of each analysis, an essential step to avoid misleading results concerning the relative importance of flow instabilities before and after the wind product change

FIG. 9. The 1993 mean wind stress curl from the ECMWF 1000-hPa (a) reanalysis and (b) operational atmospheric products. In both, the 1979–93 ECMWF reanalysis mean has been subtracted and the Hellerman and Rosenstein (1983) annual mean added back in to create the hybrid wind set. The contour interval is 7.5 Pa m^{-1} × 10^{-8}
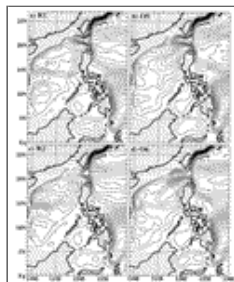
FIG. 10. The 1993 mean SSH from (a) expt 1 and (c) expt 2 forced with ECMWF reanalysis winds and from (b) expt 5 and (d) expt 6 forced by ECMWF operational winds. Experiments 5 and 6 begin from the 1992 initial state derived from expts 1 and 2 respectively. For convenience, the panels from the reanalysis (operational) winds are marked by R (O) followed by the experiment number. The contour interval is 2.5 cm